


Relaxation and dynamics of stressed predisplaced string resonatorsXiong Yao ¹, David Hoch ^{1,2,3} and Menno Poot ^{1,2,3,*}¹*Department of Physics, Technical University Munich, Garching, Germany*²*Munich Center for Quantum Science and Technology (MCQST), Munich, Germany*³*Institute for Advanced Study, Technical University Munich, Garching, Germany* (Received 5 May 2022; revised 4 October 2022; accepted 12 October 2022; published 21 November 2022)

Predisplaced micromechanical resonators made from stressed materials give rise to new static and dynamic behavior, such as geometric tuning of stress. Here, an analytical model is presented to describe the mechanics of such predisplaced resonators. The bending and tension energies are derived and a modified Euler-Bernoulli equation is obtained by applying the least action principle. By projecting the model onto a cosine shape, the energy landscape is visualized, and the predisplacement dependence of stress and frequencies is studied semianalytically. The analysis is extended with finite-element simulations, including the mode shapes, the role of overhang, the stress distribution, and the impact of film stress on beam relaxation.

DOI: [10.1103/PhysRevB.106.174109](https://doi.org/10.1103/PhysRevB.106.174109)**I. INTRODUCTION**

Nowadays, micro- and nanomechanical resonators are widely used for a large variety of applications, ranging from sensing and detection [1–3], optical and microwave quantum transducers in hybrid optoelectromechanical systems [4], to fundamental experiments in the quantum regime [5–7]. These resonators are often made out of prestrained films, such as Si₃N₄, as such materials provide very high quality factors [8–11], enabling, e.g., high detection efficiencies in the case of sensors [3] and long coherence times in mechanical quantum storage [12]. For all these experiments, it is imperative to engineer the geometry of the resonator [9,13–18] including the stress [19,20], to reach the best performance. Our recent work [21] experimentally demonstrates the geometrical tuning of the stress of resonators made out of prestrained SiN films. There, the stress in string resonators could be varied by a factor of 40, resulting in strong frequency tuning and changes in dissipation. The latter was successfully modeled using the framework of dissipation dilution [10,22], which enabled a new approach for systematic studies of the damping mechanisms in these systems. More generally, the stress reduction also allows a range of applications where stress tuning can be employed, such as matching the resonance frequencies of distinct oscillators for optomechanical synchronization [15,23,24], reducing the spring constant to enhance the signal from micromechanical sensors, or, e.g., improving the performance of optomechanical phase shifters as shown in Appendix C. Still, the relatively simple predisplaced string geometry already raises many interesting questions, such as the potential for these devices to buckle and the influence of the geometry on the eigenmodes. A thorough understanding of the statics and dynamics of these structures is, however, still lacking.

Here, we provide a detailed analysis of the mechanics of predisplaced beam resonators using analytical methods, which are supported by finite-element simulations. It is found that the relaxation of the strings is governed by a competition between bending and stretching energy, and that there are many analogies between this system and buckled beams. In Sec. II the stress relaxation of straight and predisplaced stressed beams is studied, as well as their potential to buckle. In Sec. III, expressions for the bending and tension energy stored in the beam are derived. Based on this, their equations of motion, i.e., modified Euler-Bernoulli equations, are obtained in Sec. IV. For a deeper understanding, the model is projected onto the mode shape resembling the fundamental modes (Sec. V). Finally, in Sec. VI, finite elements simulations are used to validate the results and to study the mode shapes, the role of the overhang, the distribution of the stress throughout the beams, and the influence of the film stress.

II. RELAXATION**A. Relaxation of straight strings**

Nanomechanical strings are typically made by etching a thin film, most notably silicon nitride, with a large, uniform tensile stress, followed by their release from the supporting substrate. The films are typically thin (thickness $h \ll$ length L) so that the out-of-plane components [i.e., z ; see Fig. 1(a) for the coordinate system] of the stress tensor vanish ($\sigma_{iz} = \sigma_{zi} = 0$ for $i \in \{x, y, z\}$), and only in-plane tensile forces remain. For an isotropic material, there are no shear stresses $\sigma_{xy} = \sigma_{yx} = 0$ and only the components $\sigma_{xx} = \sigma_{yy} \equiv \sigma_{\text{film}}$ remain. The film stress σ_{film} is a property of the growth process and can be controlled using, e.g., the stoichiometry of the material. It is the amount of stress that remains present for two-dimensional resonators that are clamped on all sides, such as membranes [25], or when narrow (width $w \ll L$) and straight structures are patterned but still held by the supporting substrate as

*menno.poot@tum.de

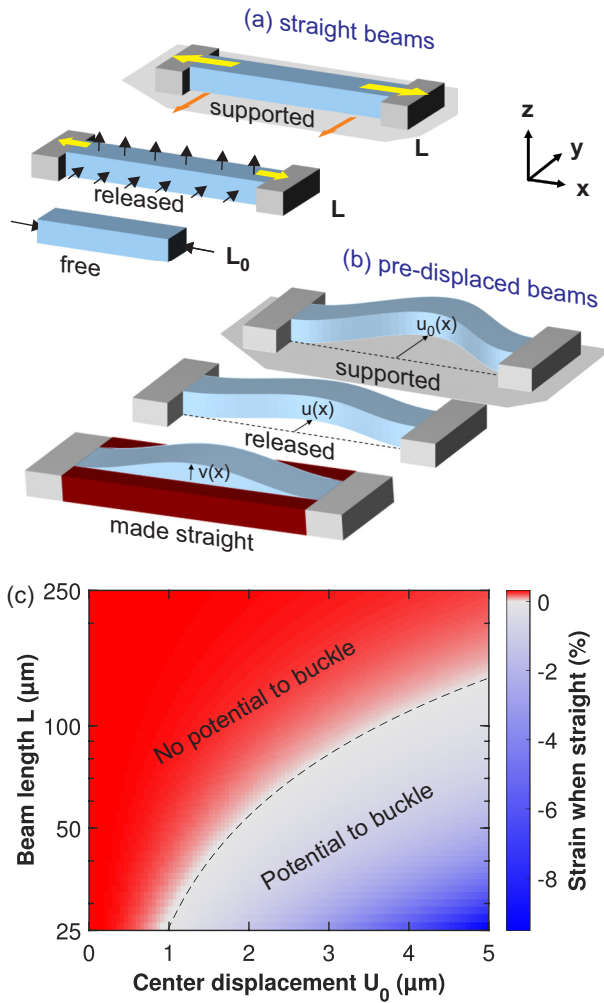


FIG. 1. (a) Illustration of the relaxation of straight strings. In the supported case (top), there is both a large stress in the x direction (yellow) and y direction (orange). After release (middle), the stress in the y direction has relaxed, resulting in shrinking in the y direction (in-plane, black arrows). For typical materials with a positive Poisson ratio, this gives rise to an expansion in the z direction (out-of-plane, black arrows) and a reduction in the stress in the x direction (yellow). The length is still the separation between the clamping points L . If the beam would be completely free (bottom), its length would reduce to L_0 and there are no stresses anymore. Here, for clarity, the transverse deformations are not shown. (b) Relaxation of pre-displaced beams. When supported (top), the beams have designed pre-displacement profile $u_0(x)$ and after release (middle) this relaxes to $u(x)$ [21]. If the beams were to be forced straight (bottom), e.g., by (fictitiously) pushing with strong structures from the sides (red), an out-of-plane buckling displacement $v(x)$ can result. (c) Color plot of the resulting strain ϵ_{xx} if the beams were made straight [as in the bottom of (b)]. Compressive (tensile) strains are indicated in blue (red) and the dashed line indicates the critical strain for out-of-plane buckling $\epsilon_{c,z}$. Note that ϵ_c is almost indistinguishable from $\epsilon = 0$. Here, $U_0 = u_0(L/2)$; for a complete list of parameters, see Appendix A.

illustrated in the top panel of Fig. 1(a). After release, the forces in the y direction cannot be sustained and $\sigma_{yy} \approx 0$ [Fig. 1(a), center]. In this case, σ_{xx} is, thus, the only remaining stress component, and we define its value as σ_0 . Since

the straight beam is clamped at the ends, the length before and after the release remains the same [see Fig. 1(a)] and thus the xx component of the strain tensor, ϵ_{xx} is identical before and after the release. For an isotropic linear-elastic material with Young's modulus E and Poisson ratio ν , this longitudinal strain is given by $\epsilon_{xx} = (\sigma_{xx} - \nu\sigma_{yy})/E$, which is $(1 - \nu)\sigma_{\text{film}}/E$ before and σ_0/E after the release. Since these two are equal, the remaining xx component of the stress tensor σ_0 can be determined: $\sigma_0 = (1 - \nu)\sigma_{\text{film}}$. For our silicon nitride films with $\sigma_{\text{film}} = 1050$ MPa and $\nu = 0.23$, this yields $\sigma_0 = 809$ MPa (see Appendix A), corresponding to a prestrain $\epsilon_{xx} = \sigma_0/E = 0.31\%$. Note that the cross-sectional area $A = hw$ can always be used to convert back and forth between the stress σ_{xx} and tension $T = \sigma_{xx}A$.

Finally, when the clamping at $x = 0$ and $x = L$ would be removed [Fig. 1(a), bottom], the beam would relax completely so that also $\sigma_{xx} = 0$, and the beam would attain a length $L_0 = (1 - \epsilon_{xx})L$. To put this into perspective: a $100 \mu\text{m}$ long beam would shrink by $L - L_0 = 310$ nm when freed.

B. Relaxation of pre-displaced strings

So far, the discussion of relaxation of stressed beams has focused on straight strings. Figure 1(b) shows a schematic of our pre-displaced strings [21]. Here, the beam is made with a center line that is not straight, but has an x -dependent displacement in the y direction $u_0(x)$. The length of the beam is thus longer than the distance between the clamping points L ; the exact length ℓ depends both on L and $u_0(x)$ as will be shown in the next section. Before release, the beam is supported [Fig. 1(b), top] and the stress is again σ_{film} . Now, upon release both transverse relaxation, as well as straightening of its shape will occur. Both will happen together, but for the understanding it is good to imagine this as two separate steps: one where the transverse stress relaxes as was shown in Fig. 1(a), but still retaining the pre-displacement, and a second one where the pre-displacement relaxes too. After the first step, the relaxed stress would also be $\sigma_0 = (1 - \nu)\sigma_{\text{film}}$, just like for a straight beam, but now along the direction of the center line, which can be locally under an angle with the x axis. There will thus be an uncompensated y component in the tension along the string, which will cause the straightening. This changes the profile from $u_0(x)$ to $u(x)$ [Fig. 1(b), middle]. As will be detailed in the following sections, how much the string straightens depends on the competition between tension and bending energy, and if there is potential to buckle.

C. Potential to buckle

Buckling is the sudden deformation of a structure under a compressive load, which can lead to out-of-plane deformations [26–28]. In engineering, buckling may result in catastrophic failure of structures, but in micromechanics buckling can also be harnessed to implement a variety of functions in micromechanical devices, e.g., for information storage [29,30] or to control propagation of waves [31]. As explained above, when pre-displaced strings relax towards the line connecting the clamping points, their curve length shortens and the tensile stress decreases. When the string would be (actively made) straight between the clamping points [see

Fig. 1(b), bottom], the tension can become negative, and out-of-plane deformations, cf. buckling in the z direction, may be energetically favorable compared to in-plane deformations for $h < w$. In this section it is explored if this situation can occur, or not.

The curve length ℓ of the resonator depends on the in- and out-of-plane displacement profiles, $u(x)$ and $v(x)$, respectively, through the functional

$$\ell[u, v] = \int_0^L \left[1 + \left(\frac{\partial u}{\partial x} \right)^2 + \left(\frac{\partial v}{\partial x} \right)^2 \right]^{1/2} dx. \quad (1)$$

Throughout this paper, it is assumed that the displacements are not large, e.g., $|u_0(x)| \ll L$ and $|\partial u_0/\partial x| \ll 1$ and likewise for u and v . In this approximation, the length becomes

$$\ell[u, v] \approx L + \frac{1}{2} \int_0^L \left(\frac{\partial u}{\partial x} \right)^2 + \left(\frac{\partial v}{\partial x} \right)^2 dx. \quad (2)$$

Now, if the string would be completely straight [cf. $u(x) = 0$ and $v(x) = 0$], then the curve length should equal the distance between the clamping points: $\ell[0, 0] = L$, which is not necessarily equal to the length that the straightened string would have if it was not clamped, L_0 , thus resulting in a strain $\epsilon_{xx} = (L - L_0)/L$ that can be positive or negative, depending on whether L_0 is smaller or larger than L . For $L_0 < L$ there is still tensile strain and no buckling occurs. However, if $L_0 > L$ there would be a compressive load exerted by the clamping points. Still, out-of-plane buckling may only occur when that compression is large enough, i.e., when the critical strain $\epsilon_{c,z} = -4\pi^2 h^2 / \{12L^2(1 - \nu^2)\} < 0$ [32] is exceeded: $(L - L_0)/L < \epsilon_{c,z}(L)$.

Figure 1(c) shows a color plot of the strain when beams with varying length L and varying predisplacements $u_0(x) = \frac{1}{2}U_0[1 - \cos(2\pi x/L)]$ would be made straight, as well as the line where the critical strain $\epsilon_{c,z}$ is reached (dashed line). Long beams with small initial displacements (top left corner) still have tensile strain when made straight, but short beams with a large displacement (bottom right corner) would have compressive strain that can exceed the critical strain. Even though in Fig. 1(c) there was a large tensile stress present before release, this shows that there are still beams that have the potential to buckle, and, thus, also the out-of-plane displacement v should be taken into account in the analysis.

III. BENDING AND TENSION ENERGY

To understand the statics and dynamics of the predisplaced strings, the potential energy that is stored in both the bending and stretching of the beam is needed. In this section, first the bending energy E_B is calculated, followed by the tension energy E_T .

A. Bending energy

It costs energy to deform a mechanical structure and a part of that is due to bending. For example, when a doubly clamped beam is displaced downwards, in the middle its bottom surface will be stretched, whereas its top becomes compressed [33,34]. Only the neutral plane does not deform. There, not only the direction of the in-plane displacement u_x , but also the displacement-induced stretching force (concretely $\sigma_{xx} - \sigma_0$, see Secs. III B and VI C) reverses sign there, so that both in the

stretched and in the compressed area, elastic energy is stored. By averaging the work needed over the cross section of the beam, one obtains [10,32,33]

$$E_{B,z}[v(x)] = \frac{D_z}{2} \int_0^L v''^2(x) dx, \quad (3)$$

where $D_z = EI_z/(1 - \nu^2)$ is the bending rigidity (also known as the flexural rigidity) and I_z is the second moment of area, which equals $wh^3/12$ for a beam with a rectangular cross section displaced in the z direction [33]. The quotes in Eq. (3) denote derivatives with respect to x . The bending energy thus depends on the curvature of the displacement profile, $v'' = \partial^2 v/\partial x^2$, squared.

In the case of a tensionless beam with a predisplacement $u_0(x)$ in the y direction, the same argument can be used to find the bending energy for the in-plane direction:

$$E_{B,y}[u(x)] = \frac{D_y}{2} \int_0^L (u''(x) - u_0''(x))^2 dx, \quad (4)$$

with $D_y = EI_y/(1 - \nu^2)$ and $I_y = w^3h/12$. For $u(x) = u_0(x)$, the bending energy is at its minimum: $U_{B,y}[u_0(x)] = 0$ and the more the beam displaces from its initial shape the more bending energy this costs. The total bending energy E_B is the sum of $E_{B,y}$ and $E_{B,z}$.

B. Tension energy

Compared to E_B , the tension energy E_T is more subtle to calculate since, in addition to a constant component T_0 , a part of the tension T depends on the flexural displacements. First focusing on in-plane displacements $u(x)$ only, one can ask what force distribution $f_y(x)$ generates a particular $u(x)$, given a tension T . The static force balance of a string under tension is [32]

$$-T[u(x)] \times \frac{\partial^2 u}{\partial x^2} = f_y(x). \quad (5)$$

This is typically used to find the displacement for a given force distribution by solving the differential equation, but when $u(x)$ is already specified, the force per unit length that is needed to create that displacement can be obtained from Eq. (5) directly. $f_y(x)$ is thus a functional of the displacement profile. This is indicated with the notation $f_y[u(x)](x)$. Equation (5) shows that the larger the displacement, the larger the force per unit length has to be.

Physically, $f_y(x)$ originates from having to balance the tension T that tries to pull the string back to $u(x) = 0$. When incrementing the displacement, work is done against that tension, which is stored as potential energy. By summing the work required to bring the displacement from 0 to $u(x)$, and integrating over the length of the string, one obtains:

$$E_T[u(x)] = \int_0^L \int_0^{u(x)} f_y[\tilde{u}(x)](x) d\tilde{u} dx. \quad (6)$$

By using Eq. (5) and defining $\tilde{u}(x) = su(x)$, Eq. (6) can be expressed as

$$E_T[u(x)] = \int_0^L \int_0^1 -T[su(x)] \frac{\partial^2(su)}{\partial x^2} d(su) dx \quad (7)$$

$$= \int_0^L T[su(x)] ds \int_0^L -\frac{\partial^2 u}{\partial x^2} u(x) dx. \quad (8)$$

Note that the second integral in Eq. (8) only contains the final displacement profile $u(x)$ and its curvature, whereas the first integral takes the changing magnitude of the displacement and tension during the process of going from $\tilde{u} = 0$ to $\tilde{u} = u$ into account through the dummy variable s . If the tension would be independent of $u(x)$, i.e., $T[u(x)] = T_0$, then the integral over s would give $\frac{1}{2}T_0$ [10]. With the contribution because of the displacement-induced elongation of Eq. (2) included, the tension is

$$T[u(x)] = T_0 + \frac{AE}{2L} \int_0^L \left(\frac{\partial u}{\partial x} \right)^2 dx. \quad (9)$$

The second term in Eq. (9) gives an additional s^2 , so that s^4 appears in the antiderivative of the first integrand of Eq. (8). The prefactor of that term is $\frac{1}{4}$ instead of the $\frac{1}{2}$ in front of T_0 in the expression from E_T . Here, it should be emphasized again that T_0 is the tension of the straight beam $T[u(x) = 0]$, and not the tension $\sigma_0 A = T[u_0(x)]$ initially present after the transverse stress relaxation, as was detailed in Sec. II B. Still, after inserting $u(x) = u_0(x)$ into Eq. (9) and rearranging, one obtains

$$T_0 = \sigma_0 A - \frac{AE}{2L} \int_0^L \left(\frac{\partial u_0}{\partial x} \right)^2 dx. \quad (10)$$

which shows clearly that T_0 depends on the predisplacement u_0 and on the initial stress σ_0 .

After performing partial integration and realizing that the boundary terms are zero for the boundary conditions $u(0) = u(L) = 0$, the tension energy becomes:

$$E_T = \frac{1}{2} \left\{ \frac{1}{2} T_0 + \frac{1}{2} T[u(x)] \right\} \int_0^L \left(\frac{\partial u}{\partial x} \right)^2 dx. \quad (11)$$

It should be noted that the effective tension appearing between the curly brackets in E_T is neither the initial tension T_0 , nor the final tension $T[u]$, but $T_{\text{eff}} = \frac{1}{2}(T_0 + T) = T_0 + \frac{1}{2}(T[u(x)] - T_0)$. When T_{eff} is positive, $u(x) = 0$ [i.e., straight strings] is a minimum of E_T . When the effective tension is negative, $u(x) = 0$ corresponds to a maximum in E_T and buckling may occur, as explored in Sec. II C. From Eq. (9) it is clear that this requires $T_0 < 0$.

When both displacements in the y (u) and z direction (v) are present, the tension is a functional of both profiles, $T[u(x), v(x)]$, and after a similar derivation as done above for u only, the tension energy E_T becomes:

$$E_T = \frac{1}{2} T_{\text{eff}} \int_0^L \left(\frac{\partial u}{\partial x} \right)^2 + \left(\frac{\partial v}{\partial x} \right)^2 dx. \quad (12)$$

with $T_{\text{eff}} = \frac{1}{2} T_0 + \frac{1}{2} T[u, v]$.

IV. EQUATIONS OF MOTION

The equation of motion for $u(x, t)$ and $v(x, t)$ can be obtained using the formalism of Lagrangian mechanics [35]. For this, the total potential energy $E_{\text{tot}} = E_B + E_T$, as derived in the previous section, as well as the kinetic energy K are

needed. The latter is

$$K = \frac{1}{2} \rho w h \int_0^L \dot{u}^2 + \dot{v}^2 dx, \quad (13)$$

where the dot indicates a derivative with respect to time t .

To obtain the equations of motion, in short, one inserts $u \rightarrow u + \delta u$ (and likewise for δv) into the Lagrangian $\mathcal{L} = K - E_{\text{tot}}$ and linearizes in the infinitesimal virtual displacement $\delta u(x, t)$. This results in integrals containing δu , as well as its time (in K) and spatial derivatives (in E_B, E_T , and T). After performing partial integration, and setting the total change in the Lagrangian $\delta \mathcal{L}$ to zero, one obtains an equation with an integral over the beam length containing $\delta u(x, t)$ itself, but no longer its derivatives. Since $\delta \mathcal{L} = 0$ should hold for arbitrary δu , the prefactor of $\delta u(x, t)$ inside the integral should vanish at all locations x . This yields the Euler-Bernoulli equations [33,34] with tension included [10,28,36,37], but now with the fourth-order spatial derivative of $u - u_0$ instead of u :

$$\rho A \ddot{u} = -D_y \left(\frac{\partial^4 u}{\partial x^4} - \frac{\partial^4 u_0}{\partial x^4} \right) + T \frac{\partial^2 u}{\partial x^2} + f_y(x, t) \quad (14)$$

$$\rho A \ddot{v} = -D_z \frac{\partial^4 v}{\partial x^4} + T \frac{\partial^2 v}{\partial x^2} + f_z(x, t). \quad (15)$$

Here, external forces (per unit length) in the y and z direction [$f_y(x, t)$ and $f_z(x, t)$] have also been included. Note, that the actual tension $T[u, v]$ appears again [28], and not the effective tension T_{eff} that turned up as prefactor in E_T [see Eq. (12)]. This is because the virtual work δE_T done by the virtual displacement δu not only contains the direct change $T_{\text{eff}} \int_0^L u' \delta u' dx$ via the integral of Eq. (12), but also the change δT_{eff} . This is analogous to the emergence of the ac tension [37] in the description of the flexural resonances of carbon nanotubes [36] and buckled beams [26]. The fact that only T appears in the equation of motion is expected, since in a local force balance, which would also lead to Eqs. (14) and (15), it is irrelevant if the tension is due to T_0 , due to the elongation, or a combination of the two.

A dimension analysis [36] shows that $TL^2/D_y \propto (\sigma/E)(L/w)^2 \equiv \Sigma_y$ is the parameter that determines the importance of tension over bending rigidity. A resonator with $\Sigma_y \gg 1$ behaves as a string, whereas one with $\Sigma_y \ll 1$ acts as a tensionless beam. Interestingly, when the stringness [21] $\Sigma_y \gg 1$, i.e., a resonator where the tension dominates over the bending rigidity, u_0 drops out of Eq. (14). Thus, after relaxing, the predisplaced beams simply behave as strings under tension and the only effect of the predisplacement u_0 will be the geometric tuning of the tension T [21]. Irrespective of the value of Σ_y , the u_0'''' term in Eq. (14) is independent of u and v and, hence, when solving the equations of motion, that term can be viewed as an additional in-plane force per unit length $+D_y u_0''''$ that acts on the beam. Thus, to solve the static displacement and the eigenmodes, one can follow the standard approach of inserting $u(x, t) = u_{\text{dc}}(x) + u_{\text{ac}}(x, t)$ and solving for the static profile $u_{\text{dc}}(x)$ and for the eigenmodes by taking $u_{\text{ac}}(x, t) = \chi_n(x) \exp(i\omega_n t)$. In the latter case, it is important to also include the ac part of the tension [36]. Although the mode shapes $\chi_n(x)$ can be solved analytically, finding the

tension and eigenvalues ω_n typically has to be done numerically [21,36].

V. PROJECTION ONTO MODES

The full equations of motion [Eqs. (14) and (15)] are partial differential equations that govern both the spatial profile and the dynamics. Getting insights from these directly is therefore not easy. The analysis can be greatly simplified by assuming a specific displacement profile and projecting onto that mode. Of course, the better that ansatz is, the better the agreement between the dynamics calculated using the full and the reduced equations of motion will be. In our experimental work [21], the focus was on the so-called S-beam design that is close to the cosine shape. Inspired by this, we take

$$\{u_0, u, v\} = \{U_0, U, V\} \times \frac{1}{2}[1 - \cos(2\pi x/L)] \quad (16)$$

for the pre- and postrelease in-plane displacement and the out-of-plane displacement, respectively. Note that displacement profiles of the form (16) satisfy the boundary conditions for doubly clamped beams [33] and also correspond to the shape of buckled beams [32]. With a single antinode at $x = L/2$, they also resemble the shape of the fundamental in- and out-of-plane flexural modes of beams and strings. On the other hand, Eq. (16) is not expected to work well for higher modes, which have very different shapes, e.g., with nodes. For these, different projections for the static and dynamic behavior may be used [37]. Alternatively the full model [Eqs. (14) and (15)] can be solved, or finite-element simulation can be performed (Sec. VI). However, in the following we focus on the fundamental modes and use the projection of Eq. (16). Inserting it into the expression for K , E_B , E_T , and T , and performing the integration yields:

$$K = \frac{1}{2}m[\dot{U}^2 + \dot{V}^2] \times \frac{3}{8} \quad (17)$$

$$E_B = \frac{1}{2}[D_y(U - U_0)^2 + D_z V^2] \frac{1}{L^3} \times 2\pi^4 \quad (18)$$

$$E_T = \frac{1}{2} \left(\frac{1}{2}T_0 + \frac{1}{2}T \right) [U^2 + V^2] \frac{1}{L} \times \frac{1}{2}\pi^2 \quad (19)$$

$$T = T_0 + \frac{EA}{2L^2}[U^2 + V^2] \times \frac{1}{2}\pi^2, \quad (20)$$

where $m = \rho Lhw$ is the total mass of the beam [32]. The factors after the multiplication sign depend on the assumed displacement profile. If, for example, instead of $\frac{1}{2}[1 - \cos(2\pi x/L)]$, $\sin(\pi x/L)$ was chosen (i.e., the fundamental mode shape of a string, as well as the predisplacement of our sine design [21]) these factors would be $\frac{1}{2}$, $\frac{1}{2}\pi^4$, $\frac{1}{2}\pi^2$, and $\frac{1}{2}\pi^2$, respectively. In other words, for the same amount of center displacement, it would have less bending energy, but equal stretching energy and tension as well as a higher effective mass $m_{\text{eff}} = \frac{3}{8}m \rightarrow \frac{1}{2}m$. In the following, we employ on the shape given by Eq. (16) for the projection onto the modes; this agrees well with finite-element simulations as will be shown below.

A. Potential energy landscape

After the projection onto the mode shape using Eq. (16), the total potential energy is a function of the two center

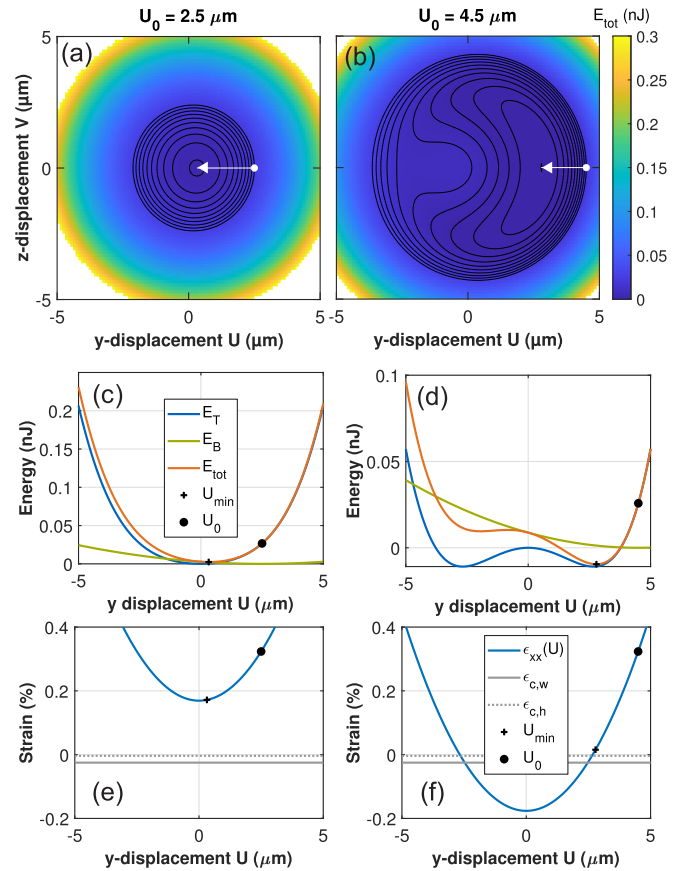


FIG. 2. Potential energy and strain of a $L = 100 \mu\text{m}$ long beam with predisplacement $U_0 = 2.5 \mu\text{m}$ (left) and $U_0 = 4.5 \mu\text{m}$ (right). The top panels show the energy landscape both as color map and with contour lines. The middle (bottom) panels show the energy (strain) for $V = 0$. The round symbols represent U_0 and the arrows and crosses indicate the minimum of E_{tot} at U_{min} . The complete list of parameter values is given in Appendix A.

displacements (U and V) only, so it is easier to visualize than the functionals of Sec. III. Figures 2(a) and 2(b) show the two-dimensional energy landscape for beams with two different center predisplacements U_0 . First of all, note that both potentials are symmetric with respect to $V = 0$. This can be understood because only V^2 appears in Eqs. (17)–(20). Moreover, both panels show that it costs energy to displace the beam beyond U_0 and that the potential energy can be lowered by straightening ($0 \leq U < U_0$). Still, the two cases show very different behavior: For $U_0 = 2.5 \mu\text{m}$, the potential energy contours appear almost concentric, and the relaxed displacement, given by the position of the potential minimum $U = U_{\text{min}}$, is close to 0. Figure 2(c) indicates that in this case the tension energy (blue) dominates over the bending energy (green) and that after straightening the string still has a considerable positive strain value [Fig. 2(e)]. For $U_0 = 2.5 \mu\text{m}$, the beam thus almost completely straightens (i.e., $U_{\text{min}} \ll U_0$) and still has considerable tensile stress after relaxing.

For $U_0 = 4.5 \mu\text{m}$, the situation is different. In this case, the potential landscape is more complex, as both the contour plot in Fig. 2(b) and the line cuts in Fig. 2(d) show. From the latter, E_{tot} appears to have two minima, but, as Fig. 2(b) shows, the

left one is actually a saddle point. The global minimum is at $U_{\min} \approx 2.79 \mu\text{m} \gg 0$, which indicates that there is still a significant displacement. In other words, the beam has not fully straightened. Looking at the strain in Fig. 2(f) clarifies that $U = 0$ would be a situation with a compressive strain that exceeds the critical value for buckling (see Sec. II C). Indeed, looking back at Fig. 1(c) shows that the beam with $U_0 = 2.5 \mu\text{m}$ does not have the potential to buckle, whereas the one with $U_0 = 4.5 \mu\text{m}$ has. In the latter case, the beam thus remains displaced, but has only very small (tensile) stress after relaxing. Note that there is no out-of-plane displacement, which would be $V_{\min} \neq 0$; in our numerical studies that situation was only encountered for compressive initial stress $\sigma_0 < 0$, but never for tensile initial stress. Thus, even for $D_y \gg D_z$, with tensile film stress the predisplaced beams prefer an in-plane displacement above out-of-plane buckling. Still, the potential to buckle as introduced in Sec. II C is an important parameter that indicates if the beams will almost completely straighten, or not.

B. Predisplacement dependence

The position of the minimum in the potential energy U_{\min} can be tracked as a function of the predisplacement U_0 . With its value, also the relaxed tension can be calculated from Eq. (20). Figures 3(a) and 3(b) show U_{\min} and the tension normalized by the cross-sectional area, respectively. These show that, in agreement with the experiments [21], for $U_0 \lesssim 3 \mu\text{m}$, the final displacement is close to zero and that the stress is still relatively large. The latter is close to that of a straight string T_0/A , as calculated using Eq. (10) (dotted). Beyond where T_0/A becomes zero, the stress becomes small, but is still tensile, and the displacement U_{\min} grows. Interestingly, the relaxed displacement approaches that of a buckled beam under compressive tension $T_0/A < 0$ (dotted line) [28]. This shows once more that the behavior of the predisplaced beams is intimately related to their potential to buckle. Before, after, and close to the buckling transition, both the final stress and displacement obtained from the analytical modal-projection model are almost indistinguishable from those obtained using finite-element simulations (FEM, dashed lines). This shows that the analytical model can be used to accurately describe the static relaxation of the predisplaced beams.

C. Reduced equations of motion

To derive the reduced equations of motion, i.e., the differential equations that govern the dynamics of the center displacements U and V , the formalism of Hamiltonian mechanics is employed. There, Hamilton's equations relate the generalized momenta P_U and P_V that are associated with U and V , respectively, to derivatives of the Hamiltonian $H = K + E_{\text{tot}}$ with respect to said quantities, and vice versa [35]:

$$P_U = + \frac{\partial H}{\partial \dot{U}} = m_{\text{eff}} \dot{U}, \quad P_V = + \frac{\partial H}{\partial \dot{V}} = m_{\text{eff}} \dot{V} \quad (21)$$

$$\dot{P}_U = m_{\text{eff}} \ddot{U} = - \frac{\partial H}{\partial U}, \quad \dot{P}_V = m_{\text{eff}} \ddot{V} = - \frac{\partial H}{\partial V}. \quad (22)$$

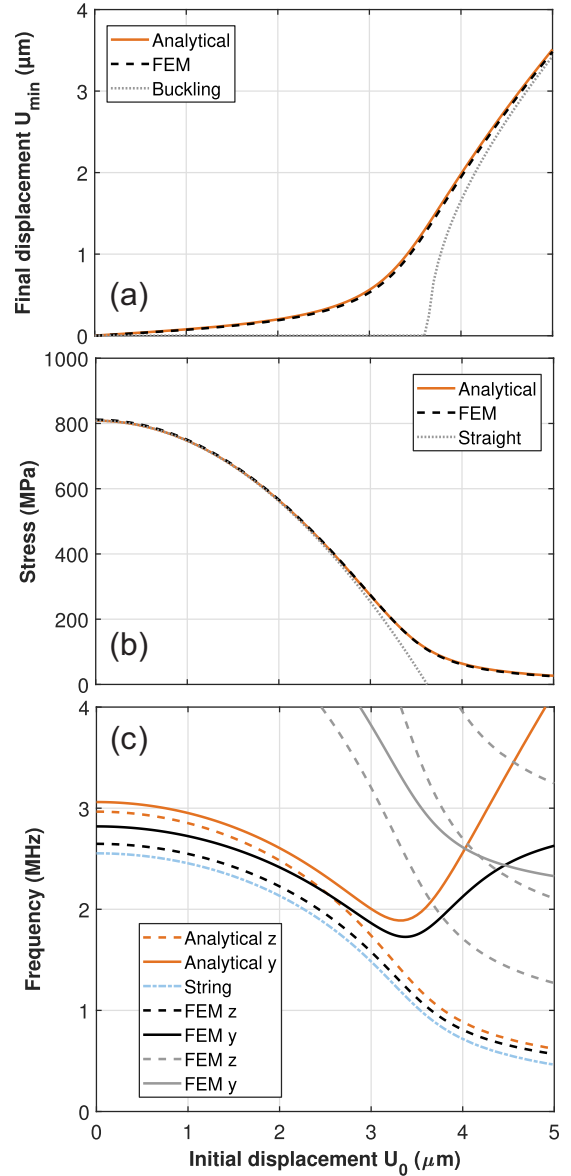


FIG. 3. (a) The final displacement U_{\min} , (b) stress, and (c) resonance frequencies as obtained using the analytical modal projection model (orange) and comparison with finite-element simulations (black) as a function of the predisplacement U_0 of a $L = 100 \mu\text{m}$ beam; other parameter values are given in Appendix A. In (a) the dotted gray line shows the displacement $2L/\pi([\sigma_{c,w} - T_0/A]/E)^{1/2}$ of a buckled beam with tension $T_0 < A\sigma_{c,w} < 0$ [32]. In (b) the stress when the beam would be straight T_0/A is also shown (dotted gray). In (c), in- (y) and out-of-plane (z) polarized modes are indicated with solid and dashed lines, respectively and the fundamental (higher) modes from the FEM simulations are indicated in black (gray). The frequencies are compared to that of a string (light blue).

From this, the reduced equations of motion follow directly:

$$m_{\text{eff}} \ddot{U} = -2\pi^4 D_y (U - U_0)/L^3 - \frac{1}{2}\pi^2 T [U, V] U/L - EA\pi^4 U^3/8L^3 \quad (23)$$

$$m_{\text{eff}} \ddot{V} = -2\pi^4 D_z V/L^3 - \frac{1}{2}\pi^2 T [U, V] V/L - EA\pi^4 V^3/8L^3. \quad (24)$$

Here, $m_{\text{eff}} = \frac{3}{8}m$ is again the effective mass, which is the same for the in- and out-of-plane mode. Comparing these equations to the equation of motion for a harmonic oscillator shows that the part of the right-hand sides that is proportional to U and V , respectively, contains the spring constants $k_{y,z}$ and these determine the resonance frequencies. Both the first (i.e., bending) and second (tension, via T_0) term contribute to this. Besides these linear contributions, there are, e.g., also terms proportional to U^3 and UV^2 . The last term in Eqs. (23) and (24) is clearly nonlinear, but, since the tension T depends on U and V [see Eq. (20)], also the second term contributes to the beam's nonlinearities. This term also nonlinearly couples in- and out-of-plane motion [37,38]; a detailed analysis of these nonlinear effects in predisplaced beams will, however, be published elsewhere.

By linearizing Eqs. (23) and (24) around $(U_{\text{min}}, V_{\text{min}} = 0)$, the spring constants $k_{y,z}$ are obtained and from these the eigenfrequencies $f = \sqrt{k_{y,z}/m_{\text{eff}}}/2\pi$.¹ Figure 3(c) shows the frequencies calculated using the analytical modal projection model as a function of U_0 in orange. Both the frequency for the z - and for the y -polarized modes show good agreement with those calculated using finite-element simulations. The vertical offset between the analytical model and the finite-element simulations may be explained by the difference between the assumed and the actual mode shape. For small U_0 , both frequencies also follow the same trend as the frequency of a string (light blue) [22,39,40] when using the tensile stress calculated with Eq. (20) [cf. the orange line Fig. 3(a)]. For larger U_0 , the z -polarized mode continues to follow the frequency of a string, but the y -polarized mode has a different behavior, both in the analytical model and the finite-element simulations. As will be shown in Sec. VIA, especially during the upward trend of the in-plane mode with U_0 , that in-plane mode shape is strongly modified, explaining why the deviation between the reduced model and the FEM simulation increases there. Still, the upward trend and the position of the transition are reproduced by the analytical model. The modal projection can thus be also used to understand the dynamics of the fundamental modes. For example, the difference between the in- and out-of-plane mode frequencies for large U_0 can be directly related to the ellipsoidal equipotential contours in Fig. 2(b) around the minimum, which indicate that the curvature of U_{tot} , i.e., the spring constants $k_{y,z}$, are very different for the V and U direction.

VI. FINITE-ELEMENT SIMULATIONS

To go beyond the analytical model presented in the previous sections and the Euler-Bernoulli equations of Eqs. (14) and (15), also finite-element (FEM) simulations were performed using COMSOL MULTIPHYSICS[®] as detailed in Appendix B and Ref. [21]. From the FEM simulations, both static and dynamic quantities can be obtained, as was shown in Fig. 3. There, there was a very good agreement between the projected model and the FEM simulations for both the final displacement and

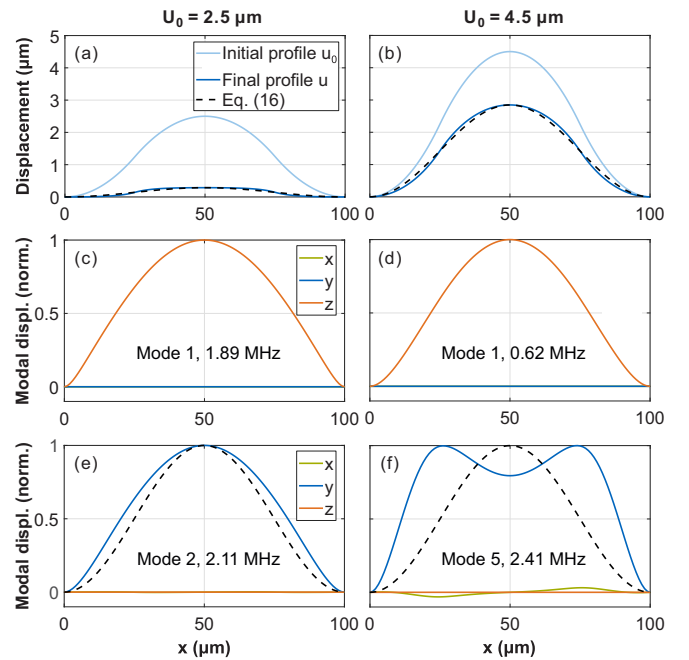


FIG. 4. Static profiles and eigenmodes of $L = 100 \mu\text{m}$ beams obtained with FEM simulations. Left panels are for $U_0 = 2.5 \mu\text{m}$ and the right ones for $4.5 \mu\text{m}$. (a) and (b) show the static displacement profile before [$u_0(x)$, light blue] and after release [$u(x)$, blue]. Corresponding normalized mode shapes of the fundamental z -polarized (c), (d) and y -polarized (e), (f) eigenmodes are illustrated, respectively. In all panels, the dashed black line indicates the cosine shape from Eq. (16) with the same maximum displacement. The different colors correspond to the different Cartesian components of the displacement vector.

the stress. For the eigenfrequencies in Fig. 3(c), deviations between the analytical model and the simulations were visible, which were attributed to the difference between the actual mode shape and the assumed cosine shape of Eq. (16). In the following, the exact mode shape will be studied in more detail using FEM simulations. Also the role of the overhanging clamping points, the stress distribution within the beams, and the effect of the film stress on beam relaxing and eigenmode will be studied in this section.

A. Mode shapes

To validate the ansatz made in Sec. V, first the static beam shape before and after relaxation is investigated. For this, the geometry of the S beam is created as detailed in Ref. [21] and its static relaxation is computed. As shown in Figs. 4(a) and 4(b), the two typical predisplaced beams that were also studied analytically, both straighten after relaxing, i.e., their final profiles $u(x)$ (blue) are smaller than the initial profile $u_0(x)$. The S beam becomes nearly straight for $U_0 = 2.5 \mu\text{m}$ while still having a significant displacement remaining for $4.5 \mu\text{m}$, which confirms the discussion from Fig. 3(a). The relaxed static profile is compared with the cosine function of Eq. (16) (dashed black line). Although the simulated profile shows slightly larger curvature near the clamping points, the two curves lie almost on top of each other, indicating that the simulated $u(x)$ is described well by the cosine shape.

¹Note that due to the symmetry with respect to $V = 0$ (see Sec. VA), there is no linear coupling ($\partial^2 E_{\text{tot}}/\partial U \partial V = 0$ for $V = 0$) between U and V and the eigenmodes are purely y and z polarized.

Next, the eigenmodes are simulated and Figs. 4(c)–4(f) show the first out-of-plane (Z1) and in-plane (Y1) polarized modes for $U_0 = 2.5 \mu\text{m}$ (left) and $4.5 \mu\text{m}$ (right). The simulated eigenfrequencies of these modes are also indicated. In both cases, the lowest eigenmode is the fundamental out-of-plane mode Z1. Taking a closer look at the mode profile shows clear differences between the two predisplacements: The left one has a finite slope close to the clamping points and looks thus more like the sine shape expected for a pure string rather than a cosine. This is not surprising, given the significant remaining stress after relaxing [see Fig. 3(b)] for this geometry [32]. By comparison, the lower final tension for $U_0 = 4.5 \mu\text{m}$ gives a larger relative bending contribution, resulting in a much more rounded shape, which is captured better by the cosine function.

For $U_0 = 2.5 \mu\text{m}$, the in-plane mode shape [Fig. 4(e)] looks similar to that of the out-of-plane mode and also resembles, but not entirely matches, the cosine shape (dashed line) of Eq. (16). However, the Y1 mode of the $U_0 = 4.5 \mu\text{m}$ beam shape looks very different [Fig. 3(f)]. The central maximum in the modal displacement is now a local minimum. Instead, two maxima appear near one and three-quarter of L . Such mode shapes are characteristic of buckled beams (see, e.g., Refs. [26,38]). Note, that Fig. 3(c) showed that at $4.5 \mu\text{m}$ predisplacement, the mode of Fig. 4(f) has crossed the y -polarized mode with a single node (Y2), similar to what happens for the aforementioned buckled beams. Hence at that point, the Y1 mode is actually the fifth eigenmode of the structure and lies above the odd Y2 mode (and also above Z1, Z2, and Z3). Still, we stick to this nomenclature as the mode in Fig. 4(f) is a direct continuation of the original Y1 at $U_0 = 0$. Irrespective of the naming, the slope and curvature are no longer accurately described by the cosine shape, explaining why the two models start to deviate beyond $U_0 \gtrsim 3.5 \mu\text{m}$ in Fig. 3(c).

All these considerations indicate that a small tension, or equivalently a large remaining U , can impact the in-plane eigenmodes due to the close connection to the dynamics of buckled beams. Note that in this case, the mode clearly deviates from the assumed cosine shape so that in this regime the analytical model from Sec. V is no longer accurate, explaining the deviations in Fig. 3(c) between that model and the FEM simulations. Still, for most of the parameters, the simulated fundamental mode shape is described to a good approximation by Eq. (16).

B. Role of overhang

Another important question is how the details of the clamping region influence the statics and dynamics of the predisplaced beams. In the experiments [21], the beams are defined by vertically etching the structures into the silicon nitride [41], followed by isotropic etching of the silicon oxide underneath. This causes an overhang of the clamping region, which can have an effect on, e.g., the residual stress and resonance frequencies [42,43]. The size of this overhang O is determined by the depth of the isotropic silicon-oxide etch and is $\sim 660 \text{ nm}$ in our experimental realization [21].

To model the role of such an overhang, the FEM geometry of the predisplaced beams is extended with two rectangu-

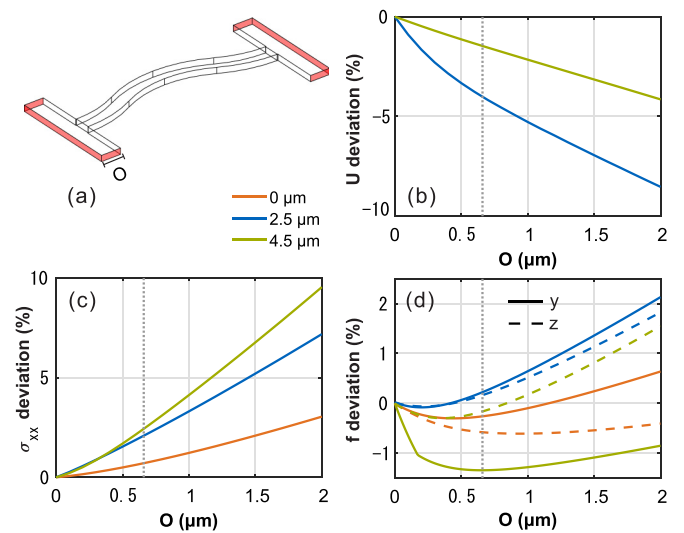


FIG. 5. Effects of overhang on three different predisplaced Sbeams' stationary and dynamical behavior. All have $L = 100 \mu\text{m}$. (a) Schematic of the geometry of an S beam with two extra overhanging clamping regions. The fixed boundaries are indicated by red color. (b) The relative change of the center displacement to the case without overhang (i.e., $[U(O) - U(O=0)]/U(O=0) \times 100\%$). (c) Relative change of the stress component σ_{xx} . (d) Relative change of the first in- (solid lines) and out-of-plane (dashed lines) eigenfrequencies. The colors correspond to different predisplacements U_0 and are consistent between the panels. The dotted gray lines indicate the etch depth of $\sim 660 \text{ nm}$ in our experiments [21].

lar pads that are clamped at their outside sides, as shown in Fig. 5(a). Their extent in the y direction is chosen large enough that the exact boundary condition at those ends does not influence the results. Intuitively, the overhang will make the clamping of the beam less rigid compared to the case with fixed boundary conditions at $x = 0, L$. This will affect the final displacement, stress, and resonance frequencies. In accordance with the previous sections, here the center displacement U is defined as the y component of the displacement vector field $\vec{u}(x, y, z)$ evaluated at the beam center: $U(O) = u_y(\frac{L}{2}, U_0, 0)|_{\text{Overhang}=O}$.² Figure 5(b) shows that for both predisplacements 2.5 and $4.5 \mu\text{m}$, the relative change in U is negative, indicating that the relaxed beams retain less final displacement when the overhang gets bigger (and for $U_0 = 0$, it stays 0). Furthermore, the residual stress component σ_{xx} shown in Fig. 5(c) increases with the overhang. The larger U_0 , the higher this relative increase of σ_{xx} is, which is consistent with the model by Bückle *et al.* [42]. In this case, the tension in the wide overhang regions pulls on the beam, thereby increasing the tension of the latter [44].

The eigenfrequencies also have a relative shift compared to a beam without overhang as Fig. 5(d) shows. However, the f change is nonmonotonic as it exhibits both downward and upward shifts. That can be understood from the interplay between the increase in effective length [43] on the one hand and the increase in the stress on the other hand. The former leads

²The Cartesian coordinates used here correspond to the original, undeformed geometry.

to a reduction in the frequency of flexural modes, whereas the latter increases the frequency [42,44]. The competition between these two effects leads to the complex behavior observed in Fig. 5(d), where, depending on displacement polarization, predisplacement, and overhang, both a positive or a negative frequency shift can be obtained. Still, the experimental etch depth of ~ 660 nm [21] will only cause small shifts of frequencies of less than $\sim 1\%$ for $100 \mu\text{m}$ string. For the stress and final displacement, the changes are slightly larger but never exceed the percent level so that in many cases its effect can be neglected. Nevertheless, for very accurate modeling of the strings, the overhang should be included.

C. Stress distribution and bending

The beam geometry has $L \gg w, h$ and in the above discussions, the beam was viewed as a one- (Sec. IV) or even zero-dimensional object (Sec. V), i.e., without considering its cross sections. Still, it is important to look how the stress of each continuum element [38] is re-distributed along the beam and over its cross section after relaxing, especially to understand better why the S beam does not become fully straight. In the following, the focus is on the xx component only, because the FEM simulations indicate that all other components are orders of magnitude of smaller (< 1 MPa) and thus negligible compared to σ_{xx} . This holds even at the largest geometric stress tuning and these simulation results thus also confirm the argument about which stress components are nonzero in Sec. II.

Figure 6 shows the σ_{xx} distribution of three different pre-displaced beams as color maps; the values averaged over the entire beam are indicated in the color bar. In agreement with Fig. 3(b), the larger U_0 , the smaller the average final stress. However, these average values do not tell the entire story as the xy projections show that locally the stress can deviate strongly from the mean. Although for the straight beam [Fig. 6(a)] the average of σ_{xx} is 811 MPa and is distributed uniformly over the structure, the stress is nonuniform for the predisplaced beams [Figs. 6(b) and 6(c)], even reaching significant negative (i.e., compressive) values for $U_0 = 4.5 \mu\text{m}$. First, note that in all cases σ_{xx} is symmetric about the center $x = L/2$. Moreover, the stress distributions at three yz planes are plotted for $U_0 = 2.5 \mu\text{m}$ [(i), (ii), and (iii)], showing that, as expected for thin beams [32,33], the stress is constant along the thickness of the beam. Therefore, slices at constant z are sufficient to fully represent the stress distribution in these structures.

The xy cuts in Figs. 6(b) and 6(c) show that for the two predisplaced beams σ_{xx} is different on both sides of the center curve (which corresponds to the so-called neutral plane [33]). Overall, the relaxation is accompanied by a shrinking of the beam's curve length as discussed in Sec. II, causing the reduction in the average longitudinal stress. On top of this global effect, one side of the beam is stretched more than average, and thus has a higher-than-average stress, whereas the other side is stretched less or even compressed, resulting in a lower local σ_{xx} that can even be compressive ($\sigma_{xx} < 0$, blue). Figure 6 shows that from 0 to $L/4$ and from $3L/4$ to L , the stress is higher at the upper edge of the xy cut and lower at the lower edge. This situation is reversed between $L/4$ and

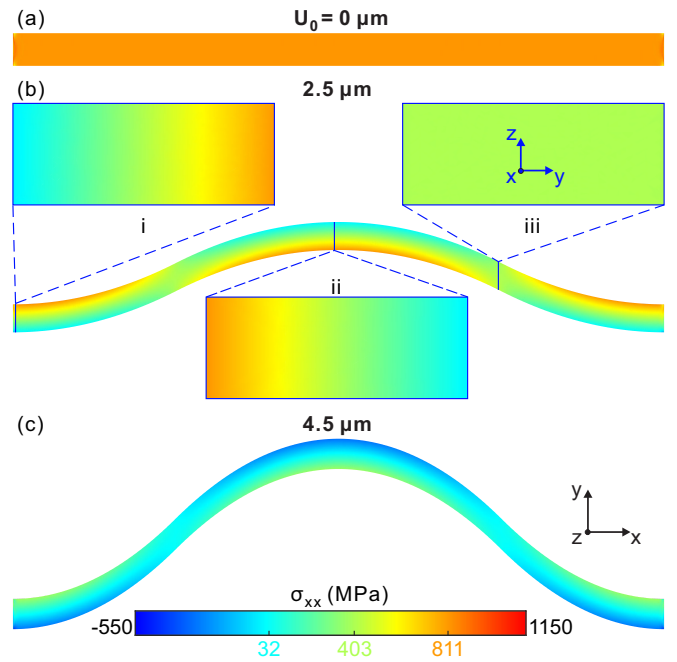


FIG. 6. Distribution of the stress component σ_{xx} for (a) $U_0 = 0$, (b) 2.5 , and (c) $4.5 \mu\text{m}$ along the beam (xy plane). The average σ_{xx} over beam is 811, 403, and 32 MPa, respectively, as indicated in the colorbar. For (b) also the stress distribution at yz cut planes are shown near a clamping point (i), halfway (ii), and at a quarter L (iii). For clarity, xy cuts have been plotted with a different vertical and horizontal scale. This may give the impression that the difference between $\ell[u_0, 0]$ and L and the angle between the center curve and the x axis are large, but in reality these are only $(\ell - L)/L = 0.17$ (0.54)% and 0.10 (0.18) rad for $U_0 = 2.5$ (4.5) μm , respectively.

$3L/4$. The border between these two regions coincides with the inflection point of the center curve. The sign of the local curvature of $u_0 - u$ thus determines whether the upper or lower side has a higher-than-average stress. A more detailed analysis of the distribution of σ_{xx} over the beam width indicates a linear dependence on y around the average value. This is exactly as expected for bending of the beam [32,33]. The FEM simulations thus confirm that the final relaxation is determined by the interplay between the tension and bending rigidity as predicted by our analytical model. Finally, it should be kept in mind that for a static situation, the longitudinal stress integrated over the width and thickness of the beam is constant along x . This can be understood since any variation of the tension $T \equiv \iint \sigma_{xx} dy dz$ leads to longitudinal displacements that will balance the gradient in T [45].

D. Film-stress dependence

A tensile film stress is a prerequisite for the straightening of predisplaced beams. This can be understood intuitively but was also shown explicitly in Sec. III. It is, thus, interesting to study how the film stress impacts the relaxation. This is an example of a parameter that is not easily varied in the experiment as would require a separate deposition run for every value [21], but can be readily changed in the analytical model

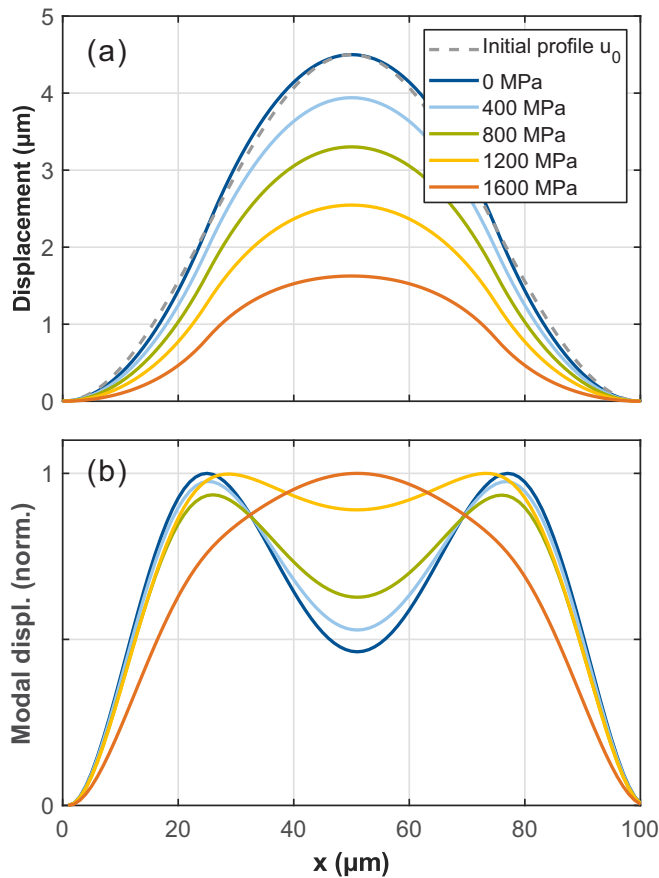


FIG. 7. Effects of film stress on S-beam relaxation and the first y -polarized eigenmode shape for $L = 100 \mu\text{m}$ and $U_0 = 4.5 \mu\text{m}$. (a) Relaxation of the S beams with different σ_{film} . The gray dashed line is the beam profile before relaxation. Others are profiles after relaxation. The colors correspond to different initial stress σ_{film} and are consistent between (a) and (b). (b) The evolution of the first y -polarized eigenmode shape showing a transition from a shapes with dip in the center to a maximum there.

as well as in the FEM simulations. The latter is presented in Fig. 7.

The beam is purely bending-rigidity dominated when $\sigma_{\text{film}} = 0$, where no relaxation occurs as is indeed visible in Fig. 7(a). In this case, the FEM simulations show that the relaxed displacement (dark blue) matches the predisplacement profile (gray). Here, $\sigma_0 = 0$ and hence $T_0 < 0$, as can be seen from Eq. (10).

Increasing the film stress reduces $u(x)$ and the beam straightens. As already illustrated in Fig. 3(a), for a given σ_{film} , the larger U_0 , the larger U but the smaller (or more negative) T_0 . On the other hand, an increase in σ_{film} increases T_0 (Sec. II), which is equivalent to the decreasing of $u_0(x)$ in Eq. (10) and vice versa. Therefore, the effect of increasing film stress on eigenfrequencies is also similar to reducing U_0 and, thus, also the film stress can be used to tune the predisplaced beams between the two regimes of Fig. 3. This can indeed be seen from the eigenmodes in Fig. 7(b), where there is a clear transition from the buckled-beam modes with a depression in the middle to the stringlike shapes with the antinode in the center. This example shows that model can

thus also be used to study the impact of parameters that are not easy to vary experimentally.

VII. CONCLUSION

A theoretical framework to analyze the relaxation and dynamics of predisplaced beams was presented. First, the relaxation of straight and predisplaced beams was studied and expressions for the bending and tension energy were derived. For the tension energy, it is neither the initial nor the final tension that appears, but their average. The equations of motion were derived and a modified Euler-Bernoulli equation is obtained. The predisplacement appears as an additional in-plane force. In the limit of high tension, the resonators behave as simple strings with a geometrically tunable tension. By projecting on the fundamental mode shape, the system is reduced to two variables: the in- and out-of-plane displacements at the center. From the energy landscape, insights in the relaxation and the role of buckling are obtained. This reduced model can be used to understand the static relaxation and dynamics of the fundamental modes, such as the geometric tuning of the stress and resonance frequencies. Finally, the analytical model is supported by finite-element simulations of the mode shapes, the role of the overhang, stress profiles, and the film stress. This enables a good understanding of the experimental observations in Ref. [21] and future work will explore the nonlinear properties of the predisplaced beams more detail.

ACKNOWLEDGMENTS

This research was funded by the German Research Foundation (DFG) under Germany's Excellence Strategy - EXC-2111-390814868 and TUM-IAS, which is funded by the German Excellence Initiative and the European Union Seventh Framework Programme under Grant Agreement No. 291763. We thank Timo Sommer and Pedro Soubelet for discussion.

APPENDIX A: PARAMETER VALUES

The parameters used are inspired by our experimental work described in Ref. [21], where high-stress silicon nitride beams were used to geometrically tune the tension and to study the dissipation in such resonators. The nominal values of the parameters used in the calculations and simulation in this paper are given in Table I.

TABLE I. Parameter values used for the calculations (unless stated otherwise).

Parameter	Description	Value	Source
h	Thickness	330 nm	[21]
w	Width	850 nm	[21]
L	Length	100 μm	[21]
σ_{film}	Film stress	1050.1 MPa	[25]
ρ	Density	$3.10 \times 10^3 \text{ kg/m}^3$	[46]
E	Young's modulus	250 GPa	[46]
ν	Poisson ratio	0.23	[46]

APPENDIX B: FINITE-ELEMENT SIMULATIONS

The FEM simulations of the predisplaced beams were first built up in the graphic user interface of COMSOL MULTIPHYSICS® (version 5.4). First, the geometry is defined in the plane geometry and extruded to three dimensions. Then, Si_3N_4 from the material library is applied to the geometry. Next, the physics of the mechanical resonators are applied under the solid mechanics. Here, e.g., the film stress is added with initial stress and strain under linear elastic material by setting σ_{xx} and σ_{yy} to 1050.1 MPa ($\sigma_{zz} = 0$). The boundary conditions for the ends are fixed under the fixed constraint. Other physics, such as external forces, can also be applied if needed. Next, the mesh is built. In this work, the default mesh element type tetrahedral was used. To study both the statics and dynamics, first the stationary solver is used, followed by the eigenfrequency solver so that the eigenmodes are calculated for the relaxed structure. Note that the setting include geometric nonlinearity has to be ticked [10] to correctly take the stress into account. For convenience with sweeping parameters and extracting and processing results, the COMSOL model was exported as a MATLAB® script, adapted to work with our simulation framework for sweeping parameters and extracting results, and executed via the MATLAB LIVELINK™. Two representative COMSOL models are available at the Zenodo open-access repository [47].

APPENDIX C: APPLICATION: IMPROVED OPTOELECTROMECHANICAL PHASE SHIFTING

As a final outlook, it is shown that our geometric tuning of stress using predisplaced structures is also applicable beyond the simple string geometry. In Fig. 8 we study an extension of our previously demonstrated optoelectromechanical phase shifter [14]. This integrated photonic device can shift the phase of light traveling through a waveguide by electrostatically displacing a mechanical structure in the shape of an H. Compared to the original design of Ref. [14], now the center of the H is displaced by an amount U_0 in the center. Upon

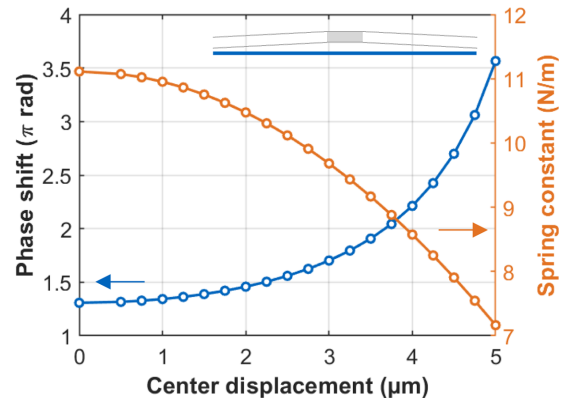


FIG. 8. Finite-element simulations of an optoelectromechanical phase shifter with a predisplacement. The left axis shows the induced phase shift for an applied force of $F = -1 \mu\text{N}$ and the right the spring constant, which is defined as $k = (\partial u_c / \partial F)^{-1}$, where u_c is the y displacement in the middle at the side of the waveguide. The inset shows the geometry where the H is designed with a $U_0 = 5 \mu\text{m}$ predisplaced away from the waveguide (blue). Other simulation parameters are as in Ref. [14] and Appendix A.

release, the structure straightens, resulting in a lower stress in the arms and thus lowering the spring constant significantly, as shown in Fig. 8. The same amount of force thus results in a much larger displacement of the optomechanical phase shifter. The resulting phase change is further amplified by the nonlinear relation between the effective refractive index and the distance between the waveguide and the phase shifter [14]. Figure 8 shows that for the same amount of applied force, the induced phase shift is more than tripled when giving the structure a predisplacement of $5 \mu\text{m}$ compared to the original design. This shows that geometric tuning of stress is not only important in the string resonators that were studied in detail in this work, but also for more general structures with a wide range of applications.

-
- [1] W. J. Westerveld, M. Mahmud-Ul-Hasan, R. Shnaiderman, V. Ntziachristos, X. Rottenberg, S. Severi, and V. Rochus, Sensitive, small, broadband and scalable optomechanical ultrasound sensor in silicon photonics, *Nature Photonics* **15**, 341 (2021).
- [2] M. Calleja, P. M. Kosaka, Á. S. Paulo, and J. Tamayo, Challenges for nanomechanical sensors in biological detection, *Nanoscale* **4**, 4925 (2012).
- [3] P. S. Waggoner and H. G. Craighead, Micro- and nanomechanical sensors for environmental, chemical, and biological detection, *Lab Chip* **7**, 1238 (2007).
- [4] N. Lauk, N. Sinclair, S. Barzanjeh, J. P. Covey, M. Saffman, M. Spiropulu, and C. Simon, Perspectives on quantum transduction, *Quantum Sci. Technol.* **5**, 020501 (2020).
- [5] A. D. O’Connell, M. Hofheinz, M. Ansmann, R. C. Bialczak, M. Lenander, E. Lucero, M. Neeley, D. Sank, H. Wang, M. Weides, J. Wenner, J. M. Martinis, and A. N. Cleland, Quantum ground state and single-phonon control of a mechanical resonator, *Nature (London)* **464**, 697 (2010).
- [6] J. Chan, T. Alegre, A. H. Safavi-Naeini, J. T. Hill, A. Krause, S. Gröblacher, M. Aspelmeyer, and O. Painter, Laser cooling of a nanomechanical oscillator into its quantum ground state, *Nature (London)* **478**, 89 (2011).
- [7] N. Fiaschi, B. Hensen, A. Wallucks, R. Benevides, J. Li, T. P. M. Alegre, and S. Gröblacher, Optomechanical quantum teleportation, *Nature Photon.* **15**, 817 (2021).
- [8] M. Poot, K. Y. Fong, and H. X. Tang, Deep feedback-stabilized parametric squeezing in an opto-electromechanical system, *New J. Phys.* **17**, 043056 (2015).
- [9] D. Høj, F. Wang, W. Gao, U. B. Hoff, O. Sigmund, and U. L. Andersen, Ultra-coherent nanomechanical resonators based on inverse design, *Nature Commun.* **12**, 1 (2021).
- [10] Q. P. Unterreithmeier, T. Faust, and J. P. Kotthaus, Damping of Nanomechanical Resonators, *Phys. Rev. Lett.* **105**, 027205 (2010).
- [11] R. Norte, J. Moura, and S. Gröblacher, Mechanical Resonators for Quantum Optomechanics Experiments at Room Temperature, *Phys. Rev. Lett.* **116**, 147202 (2016).

- [12] A. J. Heinrich, W. D. Oliver, L. M. K. Vandersypen, A. Ardavan, R. Sessoli, D. Loss, A. B. Jayich, J. Fernandez-Rossier, A. Laucht, and A. Morello, Quantum-coherent nanoscience, *Nature Nanotechnol.* **16**, 1318 (2021).
- [13] M. Eichenfield, J. Chan, R. M. Camacho, K. J. Vahala, and O. Painter, Optomechanical crystals, *Nature (London)* **462**, 78 (2009).
- [14] M. Poot and H. X. Tang, Broadband nanoelectromechanical phase shifting of light on a chip, *Appl. Phys. Lett.* **104**, 061101 (2014).
- [15] M. Bagheri, M. Poot, L. Fan, F. Marquardt, and H. X. Tang, Photonic Cavity Synchronization of Nanomechanical Oscillators, *Phys. Rev. Lett.* **111**, 213902 (2013).
- [16] G. D. Cole, I. Wilson-Rae, K. Werbach, M. R. Vanner, and M. Aspelmeyer, Phonon-tunnelling dissipation in mechanical resonators, *Nature Commun.* **2**, 231 (2011).
- [17] K. Y. Fong, D. Jin, M. Poot, A. Bruch, and H. X. Tang, Phonon coupling between a nanomechanical resonator and a quantum fluid, *Nano Lett.* **19**, 3716 (2019).
- [18] M. J. Beryhi, A. Arabmoheghi, S. A. Fedorov, A. Beccari, G. Huang, T. J. Kippenberg, and N. J. Engelsen, Perimeter Modes of Nanomechanical Resonators Exhibit Quality Factors Exceeding 10^9 at Room Temperature, *Phys. Rev. X* **12**, 021036 (2022).
- [19] A. H. Ghadimi, S. A. Fedorov, N. J. Engelsen, M. J. Beryhi, R. Schilling, D. J. Wilson, and T. J. Kippenberg, Elastic strain engineering for ultralow mechanical dissipation, *Science* **360**, 764 (2018).
- [20] A. Beccari, D. A. Visani, S. A. Fedorov, M. J. Beryhi, V. Boureau, N. J. Engelsen, and T. J. Kippenberg, Strained crystalline nanomechanical resonators with quality factors above 10 billion, *Nature Phys.* **18**, 436 (2022).
- [21] D. Hoch, X. Yao, and M. Poot, Geometric tuning of stress in silicon nitride beam resonators, *Nano Lett.* **22**, 4013 (2022).
- [22] S. Schmid, K. D. Jensen, K. H. Nielsen, and A. Boisen, Damping mechanisms in high-Q micro and nanomechanical string resonators, *Phys. Rev. B* **84**, 165307 (2011).
- [23] M. Zhang, G. S. Wiederhecker, S. Manipatruni, A. Barnard, P. McEuen, and M. Lipson, Synchronization of Micromechanical Oscillators Using Light, *Phys. Rev. Lett.* **109**, 233906 (2012).
- [24] T. Ono, K. Tanno, and Y. Kawai, Synchronized micromechanical resonators with a nonlinear coupling element, *J. Micromech. Microeng.* **24**, 025012 (2014).
- [25] D. Hoch, K.-J. Haas, L. Moller, T. Sommer, P. Soubelet, J. J. Finley, and M. Poot, Efficient optomechanical mode-shape mapping of micromechanical devices, *Micromachines* **12**, 880 (2021).
- [26] S. Etaki, M. Poot, I. Mahboob, K. Onomitsu, H. Yamaguchi, and H. S. J. van der Zant, Motion detection of a micromechanical resonator embedded in a d.c. SQUID, *Nature Phys.* **4**, 785 (2008).
- [27] S. O. Erbil, U. Hatipoglu, C. Yanik, M. Ghavami, A. B. Ari, M. Yuksel, and M. S. Hanay, Full Electrostatic Control of Nanomechanical Buckling, *Phys. Rev. Lett.* **124**, 046101 (2020).
- [28] A. H. Nayfeh, W. Kreider, and T. J. Anderson, Investigation of natural frequencies and mode shapes of buckled beams, *AIAA J.* **33**, 1121 (1995).
- [29] B. Charlot, W. Sun, K. Yamashita, H. Fujita, and H. Toshiyoshi, Bistable nanowire for micromechanical memory, *J. Micromech. Microeng.* **18**, 045005 (2008).
- [30] M. Bagheri, M. Poot, M. Li, W. P. H. Pernice, and H. X. Tang, Dynamic manipulation of nanomechanical resonators in the high-amplitude regime and non-volatile mechanical memory operation, *Nature Nanotechnol.* **6**, 726 (2011).
- [31] S. Kim, J. Bunyan, P. F. Ferrari, A. Kanj, A. F. Vakakis, A. M. van der Zande, and S. Tawfick, Buckling-mediated phase transitions in nano-electromechanical phononic waveguides, *Nano Lett.* **21**, 6416 (2021).
- [32] M. Poot and H. S. van der Zant, Mechanical systems in the quantum regime, *Phys. Rep.* **511**, 273 (2012).
- [33] A. Cleland, *Foundations of Nanomechanics* (Springer, Berlin, 2003).
- [34] L. D. Landau and E. M. Lifshitz, *Theory of Elasticity* (Butterworth-Heinemann, 1986).
- [35] D. A. Wells, *Schaum's Outline of Theory and Problems of Lagrangian Dynamics* (McGraw-Hill, New York, 1967).
- [36] M. Poot, B. Witkamp, M. A. Otte, and H. S. J. van der Zant, Modelling suspended carbon nanotube resonators, *Phys. Status Solidi B* **244**, 4252 (2007).
- [37] H. J. R. Westra, M. Poot, H. S. J. van der Zant, and W. J. Venstra, Nonlinear Modal Interactions in Clamped-Clamped Mechanical Resonators, *Phys. Rev. Lett.* **105**, 117205 (2010).
- [38] A. H. Nayfeh and D. T. Mook, *Nonlinear Oscillations* (Wiley, New York, 1979).
- [39] S. S. Verbridge, J. M. Parpia, R. B. Reichenbach, L. M. Bellan, and H. G. Craighead, High quality factor resonance at room temperature with nanostrings under high tensile stress, *J. Appl. Phys.* **99**, 124304 (2006).
- [40] A. H. Ghadimi, D. J. Wilson, and T. J. Kippenberg, Radiation and internal loss engineering of high-stress silicon nitride nanobeams, *Nano Lett.* **17**, 3501 (2017).
- [41] G. Terrasanta, T. Sommer, M. Müller, M. Althammer, R. Gross, and M. Poot, Aluminum nitride integration on silicon nitride photonic circuits: A hybrid approach towards on-chip nonlinear optics, *Opt. Express* **30**, 8537 (2022).
- [42] M. Bückle, Y. S. Klauf, F. B. Nägele, R. Braive, and E. M. Weig, Universal Length Dependence of Tensile Stress in Nanomechanical String Resonators, *Phys. Rev. Appl.* **15**, 034063 (2021).
- [43] K. Babaei Gavan, E. W. J. M. van der Drift, W. J. Venstra, M. R. Zuiddam, and van der Zant H. S. J., Effect of undercut on the resonant behaviour of silicon nitride cantilevers, *J. Micromech. Microeng.* **19**, 035003 (2009).
- [44] M. J. Beryhi, A. Beccari, S. A. Fedorov, A. H. Ghadimi, R. Schilling, D. J. Wilson, N. J. Engelsen, and T. J. Kippenberg, Clamp-tapering increases the quality factor of stressed nanobeams, *Nano Lett.* **19**, 2329 (2019).
- [45] K. Flensberg, Electron-vibron coupling in suspended nanotubes, *New J. Phys.* **8**, 5 (2006).
- [46] COMSOL material library, Si₃N₄ - Silicon nitride, COMSOL MULTIPHYSICS v5.6.
- [47] Two example COMSOL files are available on Zenodo, <https://doi.org/10.5281/zenodo.7057452>.